CrossMark

Nanocrystalline iron manganite prepared by sol–gel self-combustion method for sensor applications

Liviu Leontie[1,2] · Corneliu Doroftei[1] · Aurelian Carlescu[1]

Abstract

The nanocrystalline iron manganite was be successfully synthesized, for capacitive humidity sensor application, by sol–gel self-combustion method using polyvinyl alcohol as colloidal medium, followed by heat treatment. The best performances as humidity sensor were found, at working frequency of 100 Hz: a high sensitivity over a wide range of relative humidity, 11–98% RH (the capacity increases by over 40 times); a good linearity of the log$C$ vs. RH characteristics over the whole RH range, for all used frequencies. The sensor exhibits very small hysteresis, lower sensitivity to temperature, keeping linear characteristics and a short response time. The investigated material holds promise for humidity monitoring applications, taking into account the low cost, a wide range of relative humidity and a low-contamination impact.

1 Introduction

The adsorption of water vapors is known to enhance the surface electric conductivity and dielectric constant of the oxide compounds [1–4]. In general, humidity sensors based on oxide compounds are more chemically and thermally stable than the polymer humidity sensors [1–3]. The sensors based on conductive polymer layers and those with activated ceramic sublayer are insensitive to condensation, they display a wide measuring range, but a high temperature coefficient and, because they are pelicular, are sensitive to physical and chemical contamination.

Resistive sensors are sensitive to the impurified air with gases, which, in presence of humidity, form electrolytes (sulphur oxides, nitrogen oxides, ammonia, etc.) that can falsify the results of humidity measurement. These shortcomings are partially removed through the utilization of capacitive sensors. However, reduced variation of the total capacity with humidity, due to their generally small porosity, the difficulty to realize identical sensors, as well as the easy contamination with powders, gases or vapors, represent inherent

drawbacks the overcome of which leads to the development of new materials and methods to produce these types of sensors.

A series of oxide compounds with perovskite-type structure, simple or doped, prepared through various methods, has been investigated as materials with possible applications in resistive humidity sensors [4–11]. However, these types of materials have been less studied with respect to their application potential in capacitive humidity sensors.

Tripathy et al. [12] reported a study concerning a capacitive humidity sensor in the 33–95% relative humidity range (RH), using lead-free Ca, Mg, Fe, Ti-Oxide (CMFTO)-based electro-ceramics with perovskite structures synthesized by solid-state step-sintering. Upadhyay and Kavitha [13] studied the system $Ba_{1-x}La_xSnO_3$ ($x = 0.0$–0.1) in the form of discs (pellets), synthesized by the solid state ceramic method, as resistive and capacitive humidity sensors in the 10–98% relative humidity range. Agarwal et al. [14] studied the $(Ba,Sr)TiO_3$ in form of thin films synthesized by hydrothermal–electrochemical technique, as capacitive humidity sensors in the 8–98% relative humidity range.

Among investigated perovskites, iron manganite ($FeMnO_3$) is one of quite poorly studied. This compound has recently attracted a great deal of research interest due to its potential applications in electronics and catalysts [15–21]. Until now, there were no reported studies concerning its applicability as capacitive humidity sensor.

In the present paper the nanocrystalline $FeMnO_3$ perovskite was synthesized by sol–gel self-combustion method, using

✉ Corneliu Doroftei
 docorneliug@gmail.com

1 Integrated Center for Studies in Environmental Science for North-East Region, Alexandru Ioan Cuza University of Iasi, 7000506 Iasi, Romania
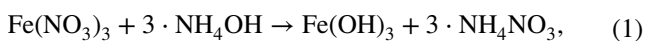
2 Faculty of Physics, Alexandru Ioan Cuza University of Iasi, 7000506 Iasi, Romania

polyvinyl alcohol as colloidal medium [22–25]. The procedure offers the advantage of producing nanosized, homogeneous and reproducible ceramic powders with high specific surface area and precise stoichiometry [26]. A major advantage of the materials realized through this method is that one obtains porous structures, including open tubular pores systems, systems favorable to vapors penetration/exhaust into the materials. From this perovskites samples/sensor elements in shape of disks with porous silver electrodes on both faces have been realized. The samples were investigated with regard to microstructural properties, as well as capacitive response to humidity in a wide range of relative humidities (0–98% RH), at different frequencies. The active surface of sensing material in contact with the humid air is very large and it is practically situated entirely inside the sensor, being thus protected against solid impurities and aerosols. So, a big amount of contaminants would be necessary for chemical contamination of the entire surface.

2 Experimental

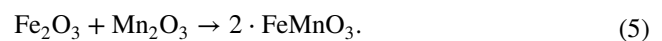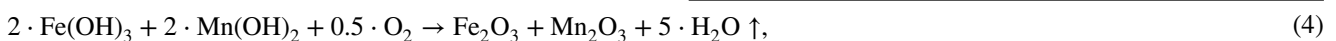### 2.1 Synthesis and characterization of materials

Nanocrystalline $FeMnO_3$ perovskite was synthesized by sol–gel self-combustion method using polyvinyl alcohol as colloidal medium. Its preparation is rather simple and inexpensive. A gel was prepared using stoichiometric amounts of analytical-grade $Fe(NO_3)_3 \cdot 9H_2O$ and $Mn(NO_3)_2 \cdot 4H_2O$ dissolved in deionized water. A solution of 10% polyvinyl alcohol was added to this nitrate solution to make a colloidal solution. The ratios of polyvinyl alcohol and metals masses were 1/1. Small amounts of NH_4OH solution (10% concentration) were dropped to adjust pH value to about 8 and a sol of metal hydroxides resulted, according to following equations:

$$Fe(NO_3)_3 + 3 \cdot NH_4OH \rightarrow Fe(OH)_3 + 3 \cdot NH_4NO_3, \quad (1)$$

$$Mn(NO_3)_2 + 2 \cdot NH_4OH \rightarrow Mn(OH)_2 + 2 \cdot NH_4NO_3. \quad (2)$$

Under stirring for 5 min a viscous gel was obtained. After drying at 120 °C, the gel was locally ignited and an exothermic combustion reaction took place:

$$C_2H_3OH + 5 \cdot NH_4NO_3 \rightarrow 2 \cdot CO_2 \uparrow + 12 \cdot H_2O \uparrow + 5 \cdot N_2 \uparrow + Q. \quad (3)$$
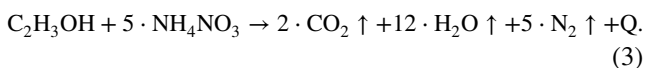
The last equation is written for one monomer molecule, vinyl alcohol. The combustion front spontaneously autopropagates through the dried gel and it converts to a loose powder. During self-combustion reaction, the metal hydroxides convert to metal oxides and the solid-state fusion of Fe_2O_3 with Mn_2O_3, to form perovskite structure, takes place:

$$2 \cdot Fe(OH)_3 + 2 \cdot Mn(OH)_2 + 0.5 \cdot O_2 \rightarrow Fe_2O_3 + Mn_2O_3 + 5 \cdot H_2O \uparrow, \quad (4)$$

$$Fe_2O_3 + Mn_2O_3 \rightarrow 2 \cdot FeMnO_3. \quad (5)$$

The resulting powders were calcined at 500 °C in air for 30 min, to eliminate any residual carbon and organic compounds. After calcination the resulting powders were subjected to cold pressing (3×10^7 N/m^2) in disk-shaped samples (17 mm diameter, 2 mm thick), followed by heat treatment in air for 5 h at 1000 °C with a heating/cooling rate of 20 °C/min. The above described method, together with applied heat treatment, allows obtaining a single phase material. We mention that the combustion reaction only is not likely capable to raise the system temperature to a level required for the perovskite synthesis.

The structural homogeneity, crystal structure, phase formation and crystallite size were determined by X-ray diffraction (XRD), using a PANanalytical X'Pert PRO MPD diffractometer and CuK_α radiation ($\lambda = 1.54251$ Å). The diffraction patterns were recorded in the range of $2\theta = 20°–80°$ at 2° min^{-1}. The average crystallite size was calculated from Scherrer's equation [27, 28]

$$D_x = \frac{0.9\lambda}{\beta \cos \theta}, \quad (6)$$

where λ is X-ray wavelength (1.54251 Å), β is the full-width at half-maximum of (222) main diffraction maximum, and θ is the Bragg diffraction angle. The X-ray density was determined from equation [22]

$$d_x = \frac{M}{Na^3}, \quad (7)$$

where M is the molecular weight, N is Avogadro's number, and a is the lattice constant.

The surface morphology was examined with a scanning electron microscope (JEOL-200CX). The specific surface area (S_{BET}) was determined from the nitrogen sorption data using the Brunauer–Emmett–Teller (BET) equation [29]. Adsorption/desorption isotherms of nitrogen were measured at 77 K using a NOVA 2200 apparatus. The pore size distribution (PSD) curves were obtained from the sorption isotherms using BJH (Barrett, Joyner and Halenda) method [29]. The chemical composition of the perovskite particles was determined with an energy dispersive X-ray spectrometer (EDX: Genesis). Incident electron beam energies from 0 to 10 keV have been used.

2.2 Sensor fabrication and measurements

The sensor element was realized by silvering both flat surfaces of heat-treated disk, using the "screen printing" method. The electric capacitance of the sample (sensor

element) was measured at 100 Hz, 1 kHz, 10 kHz and 100 kHz with a LRC METER PROTEC 9216A, using a measurement voltage of 1 V. For the humidity sensing measurements the sensor element was placed in a thermostatic enclosure at 10, 25 and 40 °C and exposed to different values of relative humidity. Relative humidities ranging from 0 to 98% were obtained using saturated salt solutions as the humidity generation sources, such as: LiCl, $K(C_2H_3O_2)$, $MgCl_2$, K_2CO_3, $Mg(NO_3)_2$, $CoCl_2$, NaCl, KCl, K_2SO_4. The dry calcium chloride ($CaCl_2$) was used to obtain dry air (0% RH) [7, 30]. The response time of samples to humidity variation was obtained by monitoring the capacitance variations when the relative humidity varied from 53 to 98% and back.

3 Results and discussion

3.1 Structure and morphology

Figure 1a, b shows the XRD patterns for samples calcined and heat treated at 900 °C for 10 min (a), and calcined and heat treated at 1000 °C for 5 h (b), respectively. Crystalline phases were identified using "Crystallographica" program. Unit cell parameters of crystalline phases were determined with XLAT-cell Refinement program. Referring to the PDF card No. 75–894, the compound exhibits a cubic symmetry (space group *la*3). The samples calcined and heat treated at 900 °C for 10 min exhibit $FeMnO_3$ perovskite phase, together with several secondary phases (Fig. 1a). This XRD pattern suggests that the annealing temperature must be

Fig. 1 XRD patterns of samples heat treated at 900 °C for 10 min (**a**), and heat treated at 1000 °C for 5 h (**b**)

higher than 900 °C. The broadened diffraction peaks indicate that very fine crystallites are present. After the heat treatment at 1000 °C for 5 h, well-defined sharp peaks can be observed in the diffraction pattern (Fig. 1b), indicating a good crystalline quality of the sample, without presence of foreign phases. The longer time interval of 5 h was preferred for the following main reasons. The heat released by the combustion reaction is not sufficient to give a suitable temperature for the synthesis of perovskite material. Besides, $FeMnO_3$ is an oxide compound and it is quite possible that the migration of ions required for the formation of perovskite structure demands some residence time at high temperature.

Table 1 includes the structural parameters of the $FeMnO_3$ samples, heat treated at 1000 °C for 5 h. As-determined lattice constant ($a = 9.400$ Å) is in good agreement with the value reported in the literature by other authors [31, 32].

Figure 2a, b shows the SEM micrographs, at two different magnifications, of the $FeMnO_3$ sample after the heat treatment at 1000 °C for 5 h. Generally, the sample is characterized by a fine granulation and a porous structure. The clustering of the particles into mini- or macro-agglomerations with irregular shapes and sizes is obvious. The $FeMnO_3$ particles being rather small ($D_x = 59.2$ nm), a tendency towards agglomerations can be thus noticed. The grain size ranges from 100 and 500 nm. One can remark the presence of large pores distributed along the grain agglomerations, as well as of open tubular pores systems favorable to vapor penetration/exhaust into the sample.

In Fig. 3 the N_2 adsorption/desorption isotherms at 77 K are presented, which have been used to get information about the specific surface area S_{BET} and pore sizes of the studied perovskite. The characteristic isotherms (Fig. 3a) correspond to type IV in the International of Pure and Applied Chemistry (IUPAC) classification [29]. The pore size distribution (PSD) obtained from N_2 desorption isotherm by BJH method [29] is illustrated in Fig. 3b. As-determined values of pore sizes fall within the range of 2–25 nm. Using S_{BET} data, the average particle size, D_{BET},
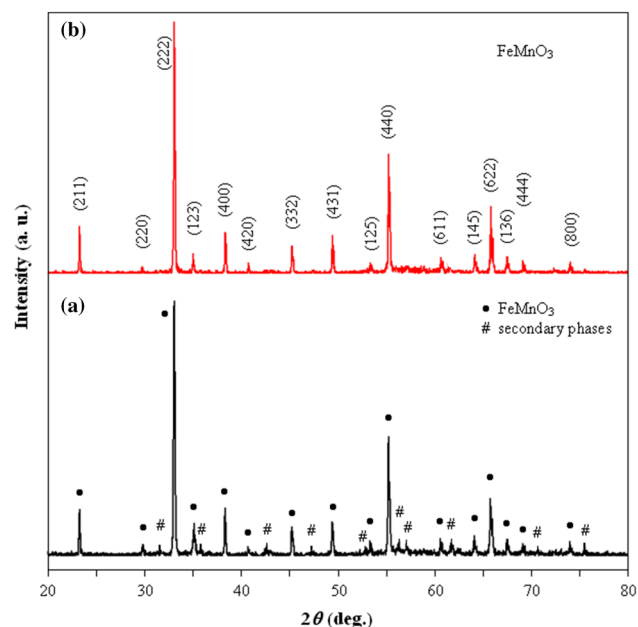
Table 1 The structural parameters and elemental analysis (EDX) of the $FeMnO_3$

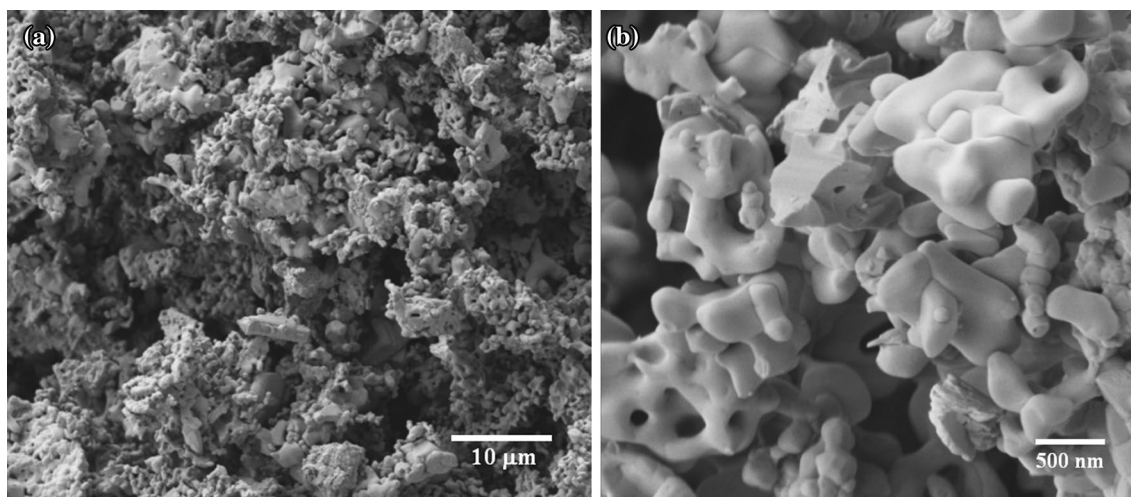|	
Lattice constant a (Å)	9.400
Average crystallite size D_x (nm)	59.2
X-ray density d_x (g/cm³)	5.08
Specific surface area S_{BET} (m²/g)	3.20
Average crystallite size D_{BET} (nm)	370
Total pore volume (cm³/g)	4.45×10^{-3}
Elemental analysis EDX	
Fe (at%)	17.25
Mn (at%)	18.98
O (at%)	63.77

Fig. 2 SEM micrographs of sample heat treated at 1000 °C for 5 h at two different magnitudes: scale 10 μm (**a**) and 500 nm (**b**)
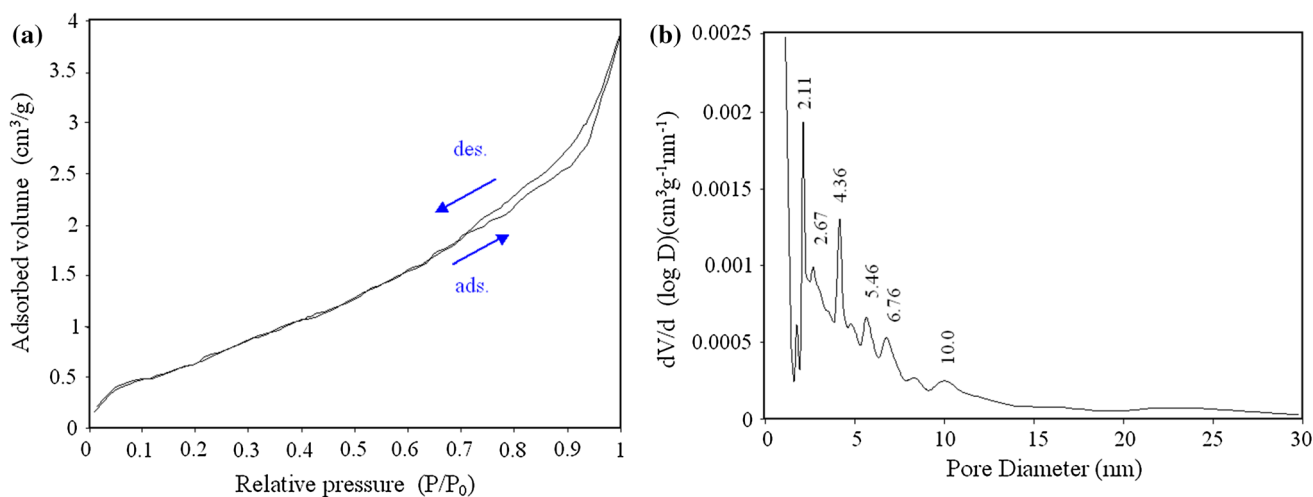

Fig. 3 Adsorption/desorption isotherm hysteresis loops (**a**), pore-size distribution curve (**b**)

was calculated with the formula (8) [29, 33] (by assuming that the particles are cubic)

$$D_{BET} = \frac{6}{S_{BET} \times d_x},$$ (8)

where 6 is the shape factor and d_x is the X-ray density.

As can be seen in Table 1, D_{BET} is substantially greater than the X-ray crystallite size, D_x. The difference is explained by the concretion of the crystal domains forming a developed network of grain boundaries, and indicates that the comprised particles are well crystallized [34].

The crystallinity of the sample, heat treated at 1000 °C for 5 h, was confirmed by the energy dispersive X-ray (EDX) spectra. Figure 4 presents the EDX spectrum for
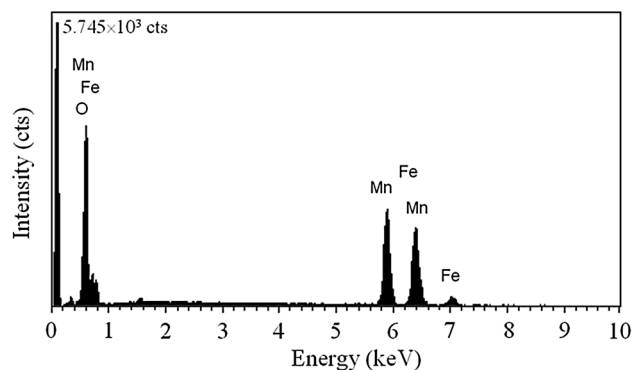

Fig. 4 EDX spectrum for FeMnO$_3$ sample

this sample. The obtained chemical elemental composition (Table 1) is typical for this perovskite (any foreign element is absent). As can be inferred, the sample composition is similar to that of nominal one, ABO_3, i.e., the $A/(A+B)$ or $B/(A+B)$ ratio is close to 0.5 (where A is Fe at%, and B is Mn at%). The method we have used offers the advantage of producing nanosized and homogeneous particles with precise stoichiometry.

3.2 Sensor properties

The capacitance of the sensor element at room temperature (25 °C), in the relative humidity range of 0–98%, was measured in the frequency range of 100 Hz–100 kHz. Figure 5 presents for comparison the log$C$ vs. RH characteristics for the sensor element at the four working frequencies (100 Hz, 1 kHz, 10 kHz and 100 kHz). One can notice that the sensor element has linear characteristics at all the frequencies between 11% and 98% RH, and the highest slope is obtained for low frequencies (100 Hz). The sensor capacitance increases with increasing RH at all measuring frequencies; at the same time, the sensor capacitance decreases with increasing working frequency.

The humidity sensitivity (S) for a given relative humidity range can be defined as [35]

$$S = \frac{C_{max}}{C_{min}} - 1, \tag{9}$$

where C_{max} and C_{min} denote the capacitances measured for the maximum and minimum values of the RH range, respectively.

Figure 6 presents the humidity sensitivity for different working frequencies, in the relative humidity range of 11–98%. The highest sensitivity value, of 436.23, is
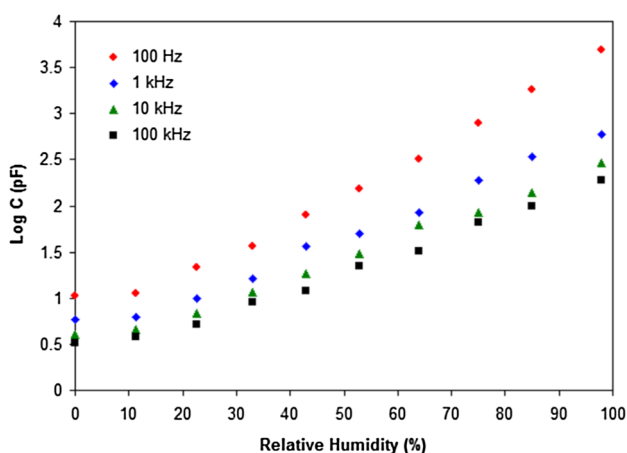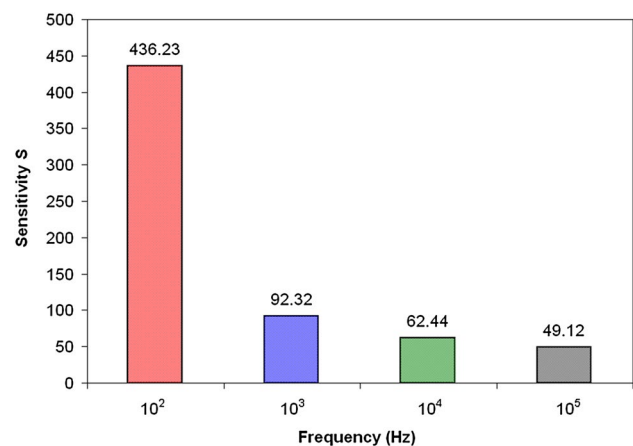

Fig. 6 Bar chart of sensitivity as a function of working frequency, for the investigated range of relative humidity, 11–98%

obtained for lower working frequency (100 Hz), and it decreases down to 49.12 at the working frequency of 100 kHz. The sensor displays a very small sensitivity, of under 0.1, within the range of 0–11% RH.

An ideal capacitive sensor exhibits a capacity value that does not depend on the working frequency. For a real sensor, this condition can be considered fulfilled in the case of very low humidity ranges. When the relative humidity of the environment to which the sensor is exposed has a higher value, the water molecules are absorbed and the sensing material exhibits a leak conduction (γ) [36]. In this conditions the capacitance (C) of the material with leak conduction can be expressed by relation (10) [12, 37]:

$$C = \varepsilon^* C_0 = \left(\varepsilon_r - i \frac{\gamma}{\omega \varepsilon_0} \right) \cdot C_0, \tag{10}$$

where ε^*, C_0 and ε_r are the complex dielectric constant, capacitance and relative dielectric constant of an ideal capacitor, respectively; ω is the angular frequency, γ denotes the conductance and ε_0 is the permittivity of free space. From Eq. (10) it results that the capacitance value decreases with increasing frequency and this decrease becomes much more prominent when RH increases. In addition, γ increases together with RH and as a result, capacitance value increases with rising RH as a function on ω [12].

The mechanism of capacity variation with humidity at a low working frequency can be explained through phenomena of adsorption (chemisorption) and absorption (physisorption) of water molecules and their effect on the variation of capacity of the system consisting of porous material and water [38, 39].

The slope of log$C$ vs. RH curve varies between a small value at low RH, and a big value above a certain RH value. At small RHs, only the adsorption phenomenon

Fig. 5 The capacity–humidity characteristics for the sensor element at four measuring frequencies

can be noticed. When only one layer of water molecules (monolayer) is adsorbed on the material surface, these are bound through two hydrogen bonds, and they cannot move in the alternating electric field, while ε_r is very small. When more layers are adsorbed on the material surface, the next layers will be bound to the inferior layer through only one hydrogen bond, molecules mobility will be larger, and ε_r will increase. When liquid water absorption also occurs, the water molecules are completely mobile, and ε_r has the large value of the bulk water [40]. Condensed water vapors occupy the entire volume of the pores with radius larger than r_K value, according to Kelvin equation [41, 42].

The log$C$ vs. RH curve initially exhibits a small slope that corresponds to an adsorbed monolayer of water, then a variable transition slope, corresponding to a bigger number of adsorbed layers, and finally, a big slope corresponding to absorbed water [2, 43, 44].

When working frequency increases, energy losses occur, due to ionic conductivity that takes place through hopping transfer of protons between adjacent hydroxyl groups, according to Grotthuss chain reaction (11) [45].

$$H_2O + H_3O^+ \rightarrow H_3O^+ + H_2O. \tag{11}$$
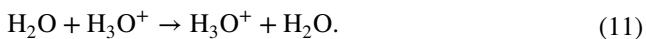
These losses result in the decrease of water complex dielectric constant, and implicitly of the slope of log$C$ vs. RH curve. The higher the working frequency, more enhanced becomes the slope decrease.

The electric capacity was measured at three temperatures, i.e., 10, 25 and 40 °C within the humidity range of 10–98% RH and at the working frequency of 100 Hz, for which the sensor sensitivity is the best. Figure 7 presents for comparison the log$C$ vs. RH characteristics for the sensor element at mentioned three measuring temperatures. One can notice an increase by below an order of magnitude of sample capacity
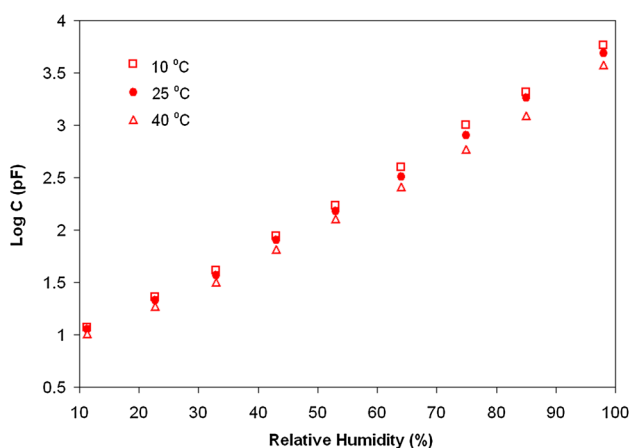
with increasing temperature within the interval of 10–40 °C, while keeping a good linearity of the characteristics. The sensor calibrated at 25 °C displays a deviation of $\pm 5\%$ RH for the temperatures of 10 °C and 40 °C. For precise measurements at extreme temperatures, it is necessary to recalibrate the measuring device.

The sensor element exhibits a good reversibility within the investigated humidity range. The maximum difference in capacitance value between the absorbtion and desorbtion curves is known as hysteresis. High hysteresis values represented a major drawback in practical humidity sensor applications. The sensor was tested at increasing and decreasing RHs and shows very small hysteresis, especially at high RHs. The capacitance hysteresis is of 0.3–3% over the whole RH range. When RH decreases, desorption of water molecules does not require much extra energy. This explains the very small hysteresis of the sensor element [3]. In Fig. 8 the adsorption and desorption curves (log$C$ vs. RH) within a narrow humidity range (85–98% RH) and at the working frequency of 100 Hz are presented.

The response time to humidity variation for the sensor element was obtained by monitoring the capacitance variations when the relative humidity changed from 53 to 98% and back. The humidity response time characteristics at 25 °C, at the frequencies of 100 Hz, 1 kHz, 10 kHz and 100 kHz, are shown in Fig. 9. The response time required for the response values to attain 90% of its maximum value are of about 3 min for adsorption (53–98% RH) and about 5 min in the case of desorption (98–53% RH). The time taken by the sensor element to come back once the water vapors concentration was reduced is found to be longer. These results suggest that the adsorption/desorption rate of water vapor is controlled by the diffusion rate of vapors through the micropores, which in turn depends on the size and distribution of large pores. One can state that, for the electric capacity of the sensor element, the humidity
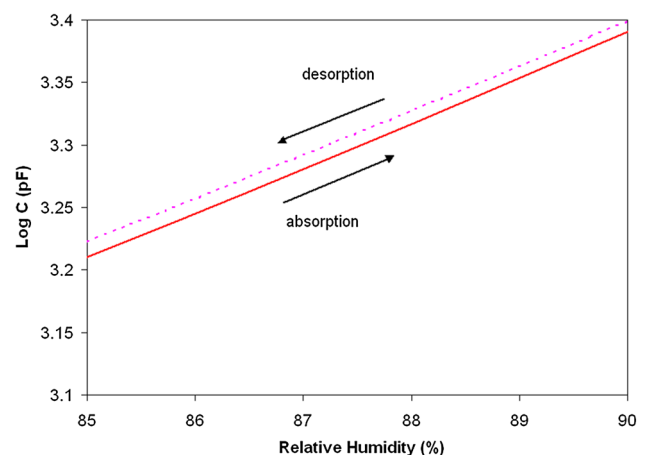

Fig. 7 The capacity–humidity characteristics for the sensor element at different temperatures; the operating frequency—100 Hz

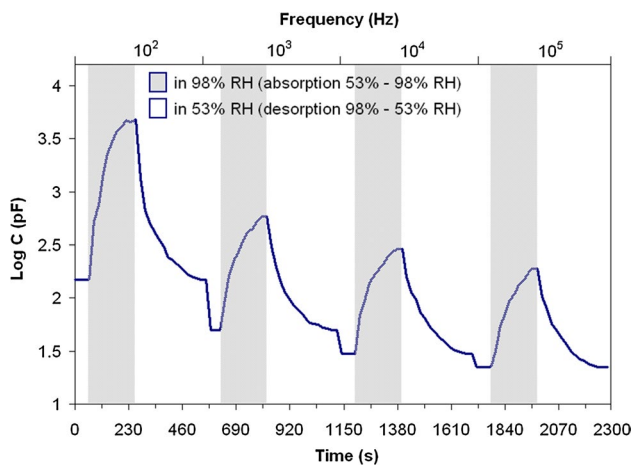**Fig. 8** The hysteresis property of the sensor at 100 Hz and 25 °C

Fig. 9 Humidity-time response characteristics for the four working frequencies

response time characteristics do not depend on the measuring frequency.

4 Conclusions

The nanocrystalline iron manganite, used as capacitive humidity sensor, can be successfully synthesized by sol–gel self-combustion method using polyvinyl alcohol as colloidal medium, followed by heat treatment for 5 h at 1000 °C. The samples exhibit a good crystallinity and a porous granular structure with average grain size of 370 nm, specific surface area of 3.20 m^2/g and total pore volume of 4.45×10^{-3} cm^3/g. The capacitive response of sensor element (disk-shaped with silver electrodes) to humidity was studied in the range of 0–98% RH at different frequencies: 100 Hz, 1 kHz, 10 kHz and 100 kHz. Sensor capacitance increases with increasing RH at all measuring frequencies and decreases with increasing working frequency. The best performances as humidity sensor were found for the $FeMnO_3$ perovskite, working at frequency of 100 Hz: a high sensitivity covering a wide range of relative humidity, between 11% and 98% RH (the capacity increases by over 40 times); a good linearity of the log$C$ vs. RH characteristics over the whole RH range, for all used frequencies. The sensor exhibits very small hysteresis, lower sensitivity to temperature, keeping linear characteristics and a short response time. The investigated oxide compound is promising for humidity monitoring, taking into account the low cost, a wide range of relative humidity and a low-contamination impact.

References

1. N. Rezlescu, E. Rezlescu, C. Doroftei, P.D. Popa, Study of some Mg-based ferrites as humidity sensors. J. Phys. Conf. Ser. **15**, 296–299 (2005)
2. E. Traversa, Ceramic sensors for humidity detection: the state-of-the-art and future developments. Sens. Actuators B **23**, 135–156 (1995)
3. Y. Wang, S. Park, J.T.W. Yeow, A. Langner, F. Müller, A capacitive humidity sensor based on ordered macroporous silicon with thin film surface coating. Sens. Actuators B **149**, 136–142 (2010)
4. H. Aria, S. Ezeki, Y. Shimizu, O. Shippo, T. Seiyama, Semiconductive humidity sensor of perovskite-type oxides. Anal. Chem. Symp. Ser. Chem. Sens. **17**, 393–398 (1983)
5. J. Holc, J. Slunecko, M. Hrovat, Temperature characteristics of electrical properties of $(Ba,Sr)TiO_3$ thick film humidity sensors. Sens. Actuators B **26–27**, 99–102 (1995)
6. Z. Wang, C. Chen, T. Zhang, H. Guo, B. Zou, R. Wang, F. Wu, Humidity sensitive properties of K^+-doped nanocrystalline $LaCo_{0.3}Fe_{0.7}O_3$. Sens. Actuators B **126**, 678–683 (2007)
7. C. Doroftei, P.D. Popa, F. Iacomi, Study of the influence of nickel ions substitutes in barium stannates used as humidity resistive sensors. Sens. Actuators A **173**, 24–29 (2012)
8. Z.A. Ansari, T.G. Ko, J.-H. Oh, Humidity sensing behavior of thick films of strontium-doped lead-zirconium-titanate. Surf. Coatings Technol. **179**, 182–187 (2004)
9. Y.C. Yeh, T.Y. Tseng, Analysis of the d.c. and a.c. properties of K_2O-doped porous $Ba_{0.5}Sr_{0.5}TiO_3$ ceramic humidity sensor. J. Mater. Sci. **24**, 2739–2745 (1989)
10. S. Ke, H. Huang, H. Fan, H.L.W. Chan, L.M. Zhou, Structural and electric properties of barium strontium titanate based ceramic composite as a humidity sensor. Solid State Ion. **179**, 1632–1635 (2008)
11. J.P. Lucaszewicz, Diode-type humidity sensor using perovskite-type oxides operable at room temperature. Sens. Actuators B **4**, 227–232 (1991)
12. A. Tripathy, S. Pramanik, A. Manna, S. Bhuyan, N.F.A. Shah, Z. Radzi, N.A.A. Osman, Design and development for capacitive humidity sensor applications of lead-free Ca, Mg, Fe, Ti-Oxides-based electro-ceramics with improved sensing properties via physisorption. Sensors **16**, 1135–1152 (2016)
13. S. Upadhyay, P. Kavitha, Lanthanum doped stannate for humidity sensor. Mater. Lett. **61**, 1912–1915 (2007)
14. S. Agarwal, G.L. Sharma, Humidity sensing properties of (Ba, Sr)TiO_3 thin films grown by hydrothermal-electrochemical method. Sens. Actuators B **85**, 205–211 (2002)
15. Z. Li, S. Wang, B. Li, X. Xiang, A new method for synthesis of $FeMnO_3$ ceramics and its phase transformation. J. Nano Res. **37**, 122–131 (2016)
16. M. Li, W. Xu, W. Wang, Y. Liu, B. Cui, X. Guo, Facile synthesis of specific $FeMnO_3$ bellow sphere/graphene composites and their superior electrochemical energy storage performances for supercapacitor. J. Power Sources **248**, 465–473 (2014)
17. K. Cao, H. Liu, X. Xu, Y. Wang, L. Jiao, $FeMnO_3$: a high-performance Li-ion battery anode material. Chem. Commun. **52**, 11414–11417 (2016)
18. S. Rayaproln, S.D. Kaushik, Magnetic and magnetocaloric properties of $FeMnO_3$. Ceram. Int. **41**, 9567–9571 (2015)
19. P. Mungse, G. Saravanan, S. Rayalu, N. Labhsetwar, Mixed oxides of iron and manganese as potential low-cost oxygen carriers for chemical looping combustion. Energy Technol. **3**, 856–865 (2015)
20. M.H. Habibi, V. Mosavi, Wet coprecipitation preparation of perovskite-type iron manganite nano powder pure phase using

nitrate precursors: structural, opto-electronic, morphological and photocatalytic activity for degradation of Nile blue dye. J. Mater. Sci. Mater. Electron. **28**, 10270–10276 (2017)

21. S.K. Kulshreshtha, S. Sharma, R. Vijayalakshmi, R. Sasikala, CO oxidation over Pd/γ-FeMnO$_3$ catalyst. Indian J. Chem. Technol. **11**, 427–433 (2004)

22. M.H. Habibi, V. Mosavi, Urea combustion synthesis of nanostructure bimetallic perovskite FeMnO$_3$ and mixed monometallic iron manganese oxides: effects of preparation parameters on structural, opto-electronic and photocatalytic activity for photodegradation of Basic Blue 12. J. Mater. Sci. Mater. Electron. **28**, 8473–8479 (2017)

23. C. Doroftei, P.D. Popa, F. Iacomi Selectivity between methanol and ethanol gas of La–Pb–Fe–O perovskite synthesized by novel method. Sens. Actuators A **190**, 176–180 (2013)

24. C. Doroftei, P.D. Popa, F. Iacomi, L. Leontie, The influence of Zn^{2+} ions on the microstructure, electrical and gas sensing properties of La$_{0.8}$Pb$_{0.2}$FeO$_3$ perovskite. Sens. Actuators B **191**, 239–245 (2014)

25. C. Doroftei, L. Leontie, Synthesis and characterization of some nanostructured composite oxides for low temperature catalytic combustion of dilute propane. RSC Adv. **7**, 27863–27871 (2017)

26. N. Rezlescu, P.D. Popa, E. Rezlescu, C. Doroftei, Microstructure characteristics of some polycrystalline oxide compounds prepared by sol–gel-selfcombustion way for gas sensor applications. Rom. J. Phys. **53**, 545–555 (2008)

27. C. Doroftei, L. Leontie, A. Popa, The study on nanogranular system manganites La–Pb–Ca–Mn–O which exhibits a large magnetoresistance near room temperature. J. Mater. Sci. Mater. Electron. **28**, 12891–12897 (2017)

28. H. Klung, L. Alexander, *X-ray diffraction procedures* (Wiley, New York, 1962)

29. B.D. Cullity, R.S. Stock, *Elements of X-ray diffraction*, 3rd edn. (Prentice Hall, New Jersey, 2001)

30. S. Lowell, J.E. Shields, M.A. Thomas, M. Thommes, *Characterization of porous solids and powders: surface area, pore size and density* (Kluwer, Dordrecht, 2004)

31. N. Rezlescu, C. Doroftei, E. Rezlescu, P.D. Popa, Structure and humidity sensitive electrical properties of the Sn^{4+} and/or Mo^{6+} substituted Mg ferrite. Sens. Actuators B **115**, 589–595 (2006)

32. D. Seifu, A. Kebede, F.W. Oliver, E. Hoffman, E. Hammond, C. Wynter, A. Aning, L. Takacs, I.-L. Siu, J.C. Walker, G. Tessema, M.S. Seehra, Evidence of ferrimagnetic ordering in FeMnO$_3$ produced by mechanical alloying. J. Mag. Mag. Mater. **212**, 178–182 (2000)

33. N. Rezlescu, E. Rezlescu, P.D. Popa, E. Popovici, C. Doroftei, M. Ignat, A.C. Barbinta, Morphological and structural aspects of some ferrospinel nanopowders for catalyst applications. Dig. J. Nanomater. Biostruct. **7**, 1709–1717 (2012)

34. D.V. Ivanov, L.G. Pinaeva, E.M. Sadovskaya, L.A. Isupova, Influence of the mobility of oxygen on the reactivity of La$_{1-x}$Sr$_x$MnO$_3$ perovskites in methane oxidation. Kinetics Catal. **52**, 401–408 (2011)

35. A. Tripathy, S. Pramanik, J. Cho, J. Santhosh, N.A.A. Osman, Role of morphological structure, doping, and coating of different materials in the sensing characteristics of humidity sensors. Sensors **14**, 16343–16422 (2014)

36. J. Wang, X.H. Wang, X.D. Wang, Study on dielectric properties of humidity sensing nanometer materials. Sens. Actuators B **108**, 445–449 (2005)

37. H. Bi, K. Yin, X. Xie, J. Ji, S. Wan, L. Sun, M. Terrones, M.S. Dresselhaus, Ultrahigh humidity sensitivity of graphene oxide. Sci. Rep. **3**, 2714–2720 (2013)

38. J. Das, S.M. Hossain, S. Chahraborty, Role of parasitic in humidity sensing by porous silicon. Sens. Actuators A **94**, 44–52 (2001)

39. B.C. Yadav, R. Srivastava, C.D. Dwivedi, Synthesis and characterization of ZnO-TiO$_2$ nanocomposite and its application as a humidity sensor. Philos. Mag. **88**, 1113–1124 (2008)

40. Z. Wang, L. Shi, F. Wu, S. Yuan, Y. Zhao, M. Zhang, The sol–gel template synthesis of porous TiO$_2$ for a high performance humidity sensor. Nanotechnology **22**, 275502–275509 (2011)

41. S.J. Gregg, K.S.W. Sing, *Adsorption, surface area and porosity*, 2nd edn. (Academic Press, New York, 1982)

42. A.W. Adamson, A.P. Gast, *Physical chemistry of surfaces*, 6th edn. (Wiley-Blackwell, New York, 1997)

43. E. McCafferty, A. Zettlemoyer, Adsorption of water vapour on α-Fe$_2$O$_3$. Discuss. Faraday Soc. **52**, 239–254 (1971)

44. T. Seiyama, N. Yamazoe, H. Arai, Ceramic humidity sensors. Sens. Actuators **4**, 85–96 (1983)

45. N. Agmon, The Grotthuss mechanism. Chem. Phys. Lett. **244**, 456–462 (1995)